Title
Molecular Hallmarks of Multiparametric Magnetic Resonance Imaging Visibility in Prostate Cancer

Permalink
https://escholarship.org/uc/item/829418xf

Journal
European Urology, 76(1)

ISSN
0302-2838

Authors
Houlahan, Kathleen E
Salmasi, Amirali
Sadun, Taylor Y
et al.

Publication Date
2019-07-01

DOI
10.1016/j.eururo.2018.12.036

Peer reviewed

Molecular hallmarks of multiparametric MRI visibility in prostate cancer

Kathleen E. Houlahan[1,2,3,*], **Amirali Salmasi**[4,*], **Taylor Y. Sadun**[4], **Aydin Pooli**[4], **Ely R. Felker**[5], **Julie Livingstone**[1], **Vincent Huang**[1], **Steven S. Raman**[5], **Preeti Ahuja**[5], **Anthony E. Sisk Jr**[6], **Paul C. Boutros**[1,2,3,4,7,8,9,10,#], **Robert E. Reiter**[4,9,11,#]

[1]Ontario Institute for Cancer Research, Toronto, Canada

[2]Department of Medical Biophysics, University of Toronto, Toronto, Canada

[3]Vector Institute, Toronto, Canada

[4]Department of Urology, David Geffen School of Medicine, University of California, Los Angeles

[5]Department of Radiology, David Geffen School of Medicine at University of California, Los Angeles

[6]Department of Pathology, David Geffen School of Medicine, University of California, Los Angeles

[7]Department of Pharmacology and Toxicology, University of Toronto, Toronto, Canada

[8]Department of Human Genetics, University of California, Los Angeles

[9]Jonsson Comprehensive Cancer Center, David Geffen School of Medicine, University of California, Los Angeles

[10]Institute for Precision Health, University of California, Los Angeles

[11]Institute of Urologic Oncology, University of California, Los Angeles

Abstract

Multiparametric magnetic resonance imaging (mpMRI) has transformed management of localized prostate cancer by improving identification of clinically significant disease at diagnosis. Approximately 20% of primary prostate tumours are invisible to mpMRI, and we hypothesize that this invisibility reflects fundamental molecular properties of the tumour. We therefore profiled the genomes and transcriptomes of 40 ISUP Grade 2 tumors: 20 mpMRI invisible (PI-RADSv2 < 3) and 20 mpMRI visible (PI-RADSv2 5). mpMRI visible tumours were enriched for hallmarks

[#]Joint corresponding authors: Dr. Paul C. Boutros: Paul.Boutros@oicr.on.ca, Dr. Robert E. Reiter: RReiter@mednet.ucla.edu.
[*]Joint first authors

of *nimbosus*, an aggressive pathological, molecular and microenvironmental phenomenon in prostate cancer. These hallmarks included more genomes with more somatic mutations, increased prevalence of IDC/CA pathology and altered abundance of 102 transcripts, including overexpression of non-coding RNAs like *SCHLAP1*. Multiple snoRNAs were identified, and a snoRNA signature synergized with *nimbosus* hallmarks to discriminate visible from invisible tumours. These data suggest a confluence of aggressive molecular and microenvironmental phenomena underlie mpMRI visibility of localized prostate cancer.

Patient summary

We examined the correlation of tumor biology and MRI visibility in a group of patients with low-intermediate risk prostate cancer. We found that MRI findings are associated with biological features of aggressive prostate cancer.

Keywords

Prostate cancer; mpMRI visibility; radiogenomics; nimbosus; transcriptomics

Improved clinical risk-stratification remains a pressing concern for localized prostate cancer, with current treatment guidelines leading to both over- and under-treatment for many patients. One promising solution to this challenge is mpMRI diffusion-weighted imaging with dynamic contrast enhancement. High Prostate Imaging Reporting and Data System version 2 (PI-RADSv2) provides international standardized guidelines for scoring images on a five-point scale reflecting the likelihood of clinically significant disease, *i.e.* PI-RADSv2 1 and 5 represent very low and very high likelihood of disease, respectively[1]. PI-RADSv2 scores accurately predict clinically significant disease[2,3]. Despite many tumours being invisible to mpMRI, insight into the molecular hallmarks of mpMRI visibility is sparse. The presence of mpMRI visible ISUP grade 1 tumors and mpMRI invisible ISUP grade 5 tumors suggests functional differences between otherwise histologically-similar tumours. We therefore hypothesized that mpMRI visibility of individual tumors is driven by specific genomic features, with high PI-RADSv2 tumors preferentially harboring molecular hallmarks of aggressiveness[4].

We therefore profiled the transcriptomic and copy number profile of 40 clinically significant invisible and visible tumors, all with ISUP Grade 2 disease and treated by radical prostatectomy. Each had a pre-surgical mpMRI and final pathology revealing a solitary ISUP Grade 2 lesion larger than 1.5 cm. Twenty tumors were mpMRI invisible (PI-RADSv2: 1–2) and 20 tumors were mpMRI visible (PI-RADsv2: 5; Figure 1A; Supplementary Table 1). To avoid confounding by zonal origin, tumours of peripheral (PZ) and transition (TZ) zones were equally represented in both groups (12 PZ and 8 TZ in per group; Table 1; Supplementary Table 1). Prostate and tumor volume were weakly correlated within the two visibility states (ρ=0.35 & 0.54 for invisible and visible, respectively; Supplementary Figure 1). Indeed, clinical characteristics alone could not predict tumour visibility (AUC=0.60, 95% CI: 0.41–0.80; Supplementary Figure 1). The groups did not differ in tumor cellularity (P=0.5; Mann Whitney test; Supplementary Table 1). As expected, the percentage of Grade 4 architecture in mpMRI visible tumours was larger than that

of mpMRI invisible ones (P < 0.001; Mann Whitney test; Table 1; Supplementary Table 1). This is consistent with literature demonstrating that MRI visibility correlates with, but does not explain, Gleason Score[5,6]. Retrospective blinded review identified five patients with PI-RADSv2 3 lesions and one with a PI-RADSv2 4 lesion (Supplementary Table 1), reported inter-observer variability (κ = 0.42–0.63) for PI-RADSv2[7,8]. No mpMRI invisible tumors were re-graded as PI-RADSv2 5.

To identify molecular hallmarks of mpMRI visibility, copy number aberrations (CNAs) and mRNA abundance were profiled for each tumor; these recapitulated known subtypes (Supplementary Figure 2). RNA and CNA profiling was highly concordant with 69% of recurrently deleted genes showing decreased mRNA abundance (Supplementary Figure 3). Our sample size provided power to detect differential abundance between visibility states of 11,604 genes (power > 0.80 at |$\log_2$FC| 1; Supplementary Figure 3). Univariate analysis identified 102 transcripts differentially abundant between visible *vs* invisible tumors, with 61% more abundant in visible tumors (FDR < 0.05; Figure 1B; Supplementary Table 2). Next, we investigated if these differentially abundant transcripts were enriched in a particular pathway and determined these transcripts were not enriched in any one particular pathway. This suggests mpMRI may be a result of dysregulation of multiple pathways rather than a single one; indeed the differentially abundant transcripts included many genes involved in prostate cancer progression. For example, *ANKRD30A* (NY-BR-1), was ~200-fold more abundant in visible tumors ($\log_2$FC=7.6; FDR < 0.001; Figure 1C), and is a tumor specific antigen present in ~30% of prostate tumors that selectively activates CD8+ T-cells[9]. Similarly, the peptide hormone Relaxin 1 was ~4-fold more abundant in visible tumors (log2FC=2.4; FDR=0.02; Figure 1D), and promotes prostate cancer progression *via* increased cell motility and androgen receptor activity[10]. Conversely, the histone methyltransferase *KMT2D* ($\log_2$FC=−0.60; FDR = 0.04) and the hypoxia inducible factor *EGLN2* ($\log_2$FC=−0.86, FDR=0.02) were significantly more abundant in invisible tumors (Supplementary Figure 3).

Unexpectedly, non-coding transcripts comprised the majority of differentially abundant RNAs (57/102). In particular, snoRNAs were significantly more likely to have elevated abundance in visible tumors (OR=4.4; FDR=0.002; Fisher's Exact test; Figure 1E). Altered snoRNAs were drawn from multiple families, including three C/D box (*SNORD33, SNORD3A* and *SNORD68*), three H/ACA box (*SNORA12, SNORA37* and *SNORA54)* and one small Cajal body-specific RNA (*SCARNA5*; Supplementary Figure 4). snoRNA enrichment was independent of host gene abundance (Supplementary Figure 4). We created a snoRNA signature that accurately discriminated PI-RADs invisible tumors (AUC=0.76, 95% CI: 0.60–0.92; Figure 1F). This snoRNA signature follows a pan-cancer report that snoRNAs are significantly more abundant in tumour than matched normal tissue[11]. Moreover, independent efforts have highlighted the role of snoRNAs in tumorigensis, specifically snoRNA U50[12,13] and snoRNA 93[14]. Indeed, 2/7 of the identified snoRNAs, SNORA37 and SNORA12, were prognostic with high abundance associated with rapid biochemical recurrence in an independent intermediate risk prostate cancer cohort (HR = 2.00 & 2.00, P = 0.053 & 0.051; EGAS00001000900; Supplementary Figure 4). Finally, several other key non-coding transcripts were associated with mpMRI visibility. In particular *TERC*, which encodes the telomerase RNA component and contains a H/ACA snoRNA-

like domain at its 3' end[15], was enriched in visible tumors ($\log_2$FC=1.6; FDR=0.04; Supplementary Figure 4).

Perhaps most provocatively, *SCHLAP1*, a lncRNA linked to prostate cancer progression[16], was more abundant in visible tumors ($\log_2$FC=3.2, FDR=0.03; Figure 2A) and the increased abundance could not be explained by CNAs ($\log_2$FC=−0.39, P=0.7; Supplementary Figure 4). *SCHLAP1* abundance fell within the expected range for ISUP grade 2 prostate tumours (EGAS00001000900; Supplementary Figure 4), however, it alone could not accurately predict mpMRI visibility (AUC=0.60; 95% CI: 0.41–0.80; Supplementary Figure 4). Therefore, we next considered *nimbosus,* a phenomenon characterized by the co-occurrence of pathological, molecular and microenvironmental events, including intraductal carcinoma and cribriform architecture (IDC/CA), genomic instability, *SCHLAP1* expression and hypoxia[17]. This co-occurrence results in an aggressive tumor phenotype, with poor patient outcome. *SCHLAP1* enrichment in visible tumors suggested that *nimbosus* might be associated with mpMRI visibility, leading us to investigate its other hallmarks. We quantified genomic instability as the percentage of the genome altered *via* CNAs (PGA). PGA was elevated in visible tumors (P=0.03; β = 0.6 adjusted for tumour purity; Figure 2B), driven by longer average length of individual amplifications and deletions (Supplementary Figure 5). Concordantly, IDC/CA was enriched in visible tumors (OR = 7.0; P=0.03; Figure 2C). Cribriform architecture and intraductal carcinoma subsets were of particular interest as their visibility on mpMRI has been debated[18,19], and are associated with advanced disease[18,20] and worse disease specific survival[21,22]. Interestingly, there was no difference in hypoxia levels between the groups, regardless of gene signature used to quantify hypoxia (Figure 2D; Supplementary Figure 5). Both PGA and hypoxia measurements fell within the expected range for ISUP grade 2 prostate cancer tumors[23] (Supplementary Figure 5). These hallmarks were not driven by the five tumors with upgraded PI-RADSv2 scores upon blinded retrospective review or by the percentage of Gleason 4 in the tumor (Supplementary Figure 5). Indeed, SCHLAP1 mRNA abundance was still significantly enriched in PI-RADSv2 5 tumors after removing the upgraded invisible tumors ($\log_2$FC = 2.75, P=0.03, Mann-Whitney test), and SCHLAP1 mRNA and PGA were only weakly correlated with percent grade 4 in visible tumors (ρ = 0.33 & 0.19, P = 0.15 & 0.4, respectively, Spearman correlation; Supplementary Figure 5). Finally, because hallmarks were not strongly correlated (Supplementary Figure 6), we looked at synergy between them, and found the odds of visibility to be 10-fold higher with co-occurrence of 2 hallmarks (OR=10; P=5.7×10−3; Figure 2E). These are exploratory analyses requiring further validation. Nevertheless, nimbosus hallmarks synergized with snoRNA levels to predict visibility with 87% accuracy, superior to the 60% accuracy of a clinical signature (Supplementary Figure 1), suggesting elevated snoRNA abundance may be a novel hallmark of nimbotic tumors (AUC=0.87, 95% CI: 0.75–0.99; Figure 2F). This comprises a promising preliminary signature of mpMRI visibility for future validation studies.

Together, this work points to a novel model for the origin of mpMRI visibility involving the co-occurrence of multiple aggressive hallmarks, reminiscent of *nimbosus*. These hallmarks include IDC/CA pathology, increased PGA and overexpression of key non-coding transcripts, such as *SCHLAP1* and snoRNAs. We note that our cohort size was limited to detecting large transcriptomic alterations ($\log_2$FC 0.6; Supplementary Figure 3), and

that our single-region sampling does not fully represent the spatial heterogeneity of the tumor. The tumor area of interest were selected with the guidance of a uropathologist to reflect architecture representative of the tumor as a whole and the relevant areas of tissue were *macro-dissected* for nucleic acid extraction. While an entire tumor may not be visible (even in those tumors with PI-RADSv2 5 lesions), and invisible portions of PI-RADSv2 5 tumors included in this analysis will lead to underestimation of the molecular differences. Thus this work serves as a lower bound on the differences between visible and invisible tumours. Similarly, our study has higher power for events earlier in evolution -- those common to invisible and visible regions of tumor -- which again under-estimates true molecular differences. Finally, it is important to note that characterization of hypoxic microenvironment was conducted on surgically resected tissue. Molecular signatures of hypoxia do not account for variable operative time that could lead to non-uniform molecular degradation. *in vivo* quantification techniques, such as ultrasound-guided transrectal needle Eppendorf electrode[24], are required for more accurate characterization of hypoxic microenvironment. This work highlights the clinical utility of integrated radiogenomic models for stratifying indolent *vs* aggressive disease and presents a novel model for mpMRI visibility. These data suggest a confluence of aggressive transcriptomic, genomic and pathological hallmarks required for mpMRI visibility, providing a molecular basis for the observation that visible tumours are clinically more aggressive.

Supplementary Material

Refer to Web version on PubMed Central for supplementary material.

Acknowledgements

References

1. Weinreb JC, Barentsz JO, Choyke PL, et al. PI-RADS Prostate Imaging – Reporting and Data System: 2015, Version 2. Eur. Urol. 2016;69:16–40. [PubMed: 26427566]

2. Almeida GL, Petralia G, Ferro M, et al. Role of Multi-Parametric Magnetic Resonance Image and PIRADS Score in Patients with Prostate Cancer Eligible for Active Surveillance According PRIAS Criteria. Urol Int 2016;96:459–469. [PubMed: 27045167]

3. Kasivisvanathan V, Rannikko AS, Borghi M, et al. MRI-targeted or standard biopsy for prostate-cancer diagnosis. N Engl J Med 2018;378:1787–1777.

4. Lalonde E, Ishkanian AS, Sykes J, et al. Tumor genomic and microenvironmental heterogeneity for integrated prediction of 5-year biochemical recurrence of prostate cancer: a retrospective cohort study. Lancet Oncol 2014;15:1521–1532. [PubMed: 25456371]

5. Le JD, Tan N, Shkolyar E, et al. Multifocality and prostate cancer detection by multiparametric magnetic resonance imaging: correlation with whole-mount histopathology. Eur Urol 2015;67:569–576. [PubMed: 25257029]

6. Filson CP, Natarajan S, Margolis DJ, et al. Prostate cancer detection with magnetic resonance-ultrasound fusion biopsy: The role of systematic and targeted biopsies. Cancer 2016;122:884–892. [PubMed: 26749141]

7. Muller Bg, Shih JH, Sankineni S, et al. Prostate Cancer: Interobserver Agreement and Accuracy with the Revised Prostate Imaging Reporting and Data System at Multiparametric MR Imaging. Radiology 2015;277:741–750. [PubMed: 26098458]

8. Purysko AS, Bittencourt LK, Bullen JA, et al. Accuracy and Interobserver Agreement for Prostate Imaging Reporting and Data System, Version 2, for the Characterization of Lesions Identified on Multiparametric MRI of the Prostate. AJR Am J Roentgenol 2017;209:339–349. [PubMed: 28570099]

9. Jäger D, Karbach J, Pauligk C, et al. Humoral and cellular immune responses against the breast cancer antigen NY-BR-1: definition of two HLA-A2 restricted peptide epitopes. Cancer Immun. 2005;5:11. [PubMed: 16335914]

10. Thompson VC, Hurtado-Coll A, Turbin D, et al. Relaxin drives Wnt signaling through upregulation of PCDHY in prostate cancer. Prostate 2010;70:1134–1145. [PubMed: 20503398]

11. Gong J, Li Y, Liu CH, et al. A pan-can analysis of the expression and clinical relevance of small nucleolar RNAs in human cancer. Cell Rep. 2017;21:1968–1981. [PubMed: 29141226]

12. Dong XY, Rodriguex C, Guo P, et al. SnoRNA U50 is a candidate tumor-suppressor gene at 6q14.3 with a mutation associated with clinically significant prostate cancer. Hum. Mol. Genet. 2008;17:1031–1042. [PubMed: 18202102]

13. Dong XY, Guo P, Boyd J, et al. Implication of snoRNA U50 in human breast cancer. J. Genet. Genomics 2009;36:447–454. [PubMed: 19683667]

14. Patterson DG, Roberts JT, King VM, et al. Human snoRNA-93 is processed into a microRNA-like RNA that promotes breast cancer cell invasion. NPJ Breast Cancer 2017;3:25. [PubMed: 28702505]

15. Mitchell JR, Cheng J & Collins K. A box H/ACA small nucleolar RNA-like domain at the human telomerase RNA 3' end. Mol. Cell. Biol. 1999;19:567–76. [PubMed: 9858580]

16. Prensner JR, Iyer MK, Sahu A, et al. The long noncoding RNA SChLAP1 promotes aggressive prostate cancer and antagonizes the SWI/SNF complex. Nat. Gen. 2013;45:1392–1398.

17. Chua MLK, Lo W, Pintilie M, et al. A Prostate Cancer 'Nimbosus': Genomic Instability and SChLAP1 Dysregulation Underpin Aggression of Intraductal and Cribriform Subpathologies. Eur. Urol. 2017;72:665–674. [PubMed: 28511883]

18. Masoomian M, Downes MR, Sweet J, et al. Concordance of biopsy and prostatectomy diagnosis of intraductal and cribriform carcinoma in a prospectively collected dataset. Histopathology 2018.

19. Truong M, Hollenberg G, Weinberg E, et al. Impact of Gleason Subtype on Prostate Cancer Detection Using Multiparametric Magnetic Resonance Imaging: Correlation with Final Histopathology. J Urol 2017;198:316–321. [PubMed: 28163032]

20. Kweldam CF, Wildhagen MF, Steyerberg EW, et al. Cribriform growth is highly predictive for postoperative metastasis and disease-specific death in Gleason score 7 prostate cancer. Mod Pathol 2015;28:457–464. [PubMed: 25189638]

21. Kweldam CF, Kummerlin IP, Nieboer D, et al. Disease-specific survival of patients with invasive cribriform and intraductal prostate cancer at diagnostic biopsy. Mod Pathol 2016;29:630–636. [PubMed: 26939875]

22. Trudel D, Downes MR, Sykes J, et al. Prognostic impact of intraductal carcinoma and large cribriform carcinoma architecture after prostatectomy in a contemporary cohort. Euro J Cancer 2014;50:1610–1616.

23. Espiritu SMG, Liu LY, Rubanova Y, et al. The evolutionary landscape of localized prostate cancers drives clinical aggression. Cell 2018;173:1003–1013. [PubMed: 29681457]

24. Parker C, Milosevic M, Toi A, et al. Polarographic electrode study of tumor oxygenation in clinically localized prostate cancer. Int J Radiat Oncol Biol Phys 2004;58:750–757. [PubMed: 14967430]

Take home message

Genome-wide CNA and transcriptomic profiling of invisible and visible mpMRI tumors identified a confluence of aggressive transcriptomic, genomic and pathological hallmarks correlated with mpMRI visibility. This work provides a molecular basis for the observation that visible tumours are clinically more aggressive.
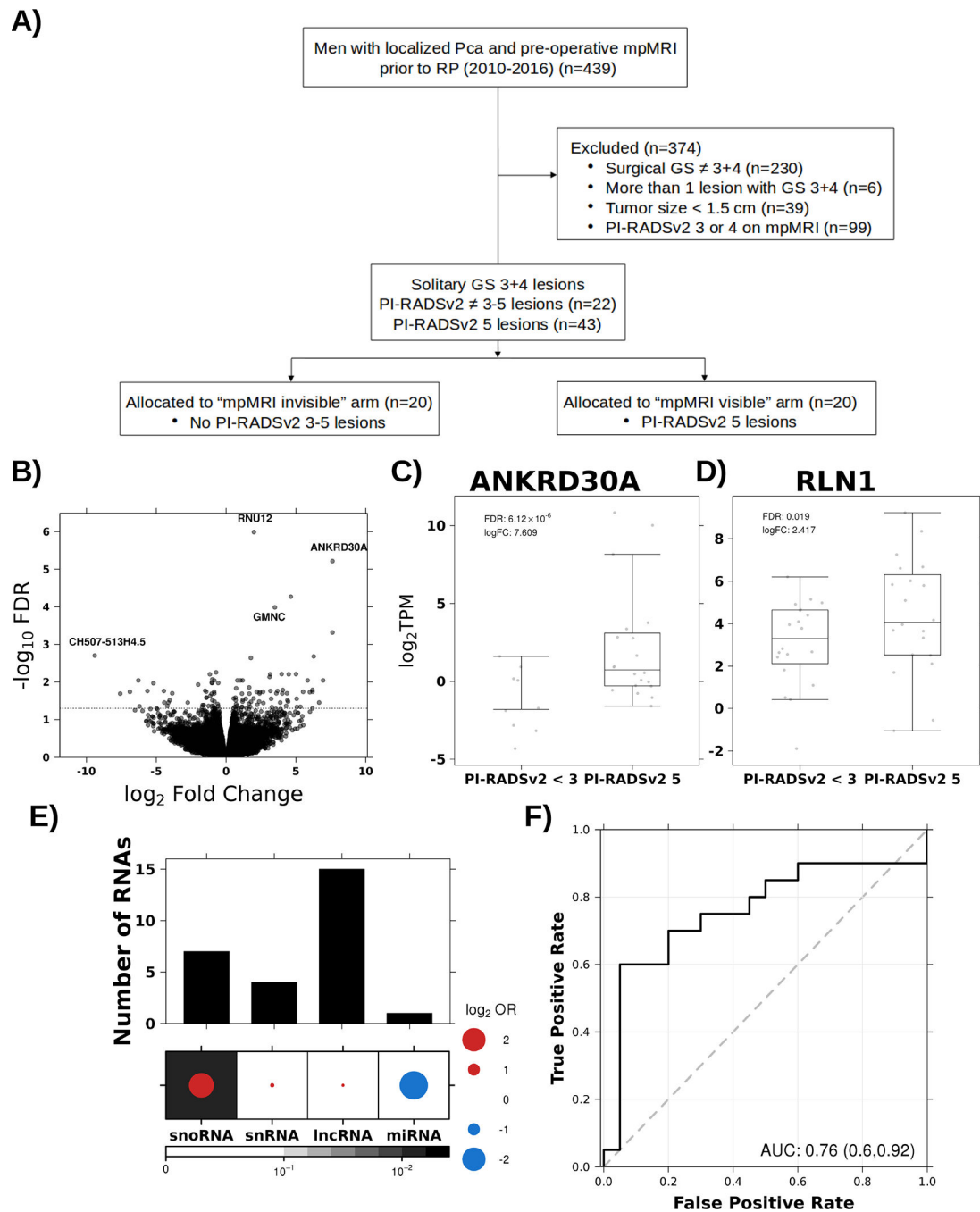
A)

B)

C) ANKRD30A

D) RLN1

E)

F)

Figure 1 - Transcriptomic basis of mpMRI visibility

A) Outline of study design, highlighting criteria for patient inclusion and exclusion.

B) Differentially abundant RNAs in PI-RADSv2 5 vs 1–2 tumors as determined from negative binomial generalized log-linear model. Horizontal dotted line indicates FDR=0.05. *ANKRD30A* (**C**) and *RLN1* (**D**) are upregulated in PI-RADSv2 5 tumors. Fold change and FDR from negative binomial generalized log-linear model and boxplots show 25% quartile, median and 75% quartile. **E)** snoRNAs were enriched in the subset of differentially abundant RNAs. The top barplot indicates the number of each non-coding RNA in the subset and the
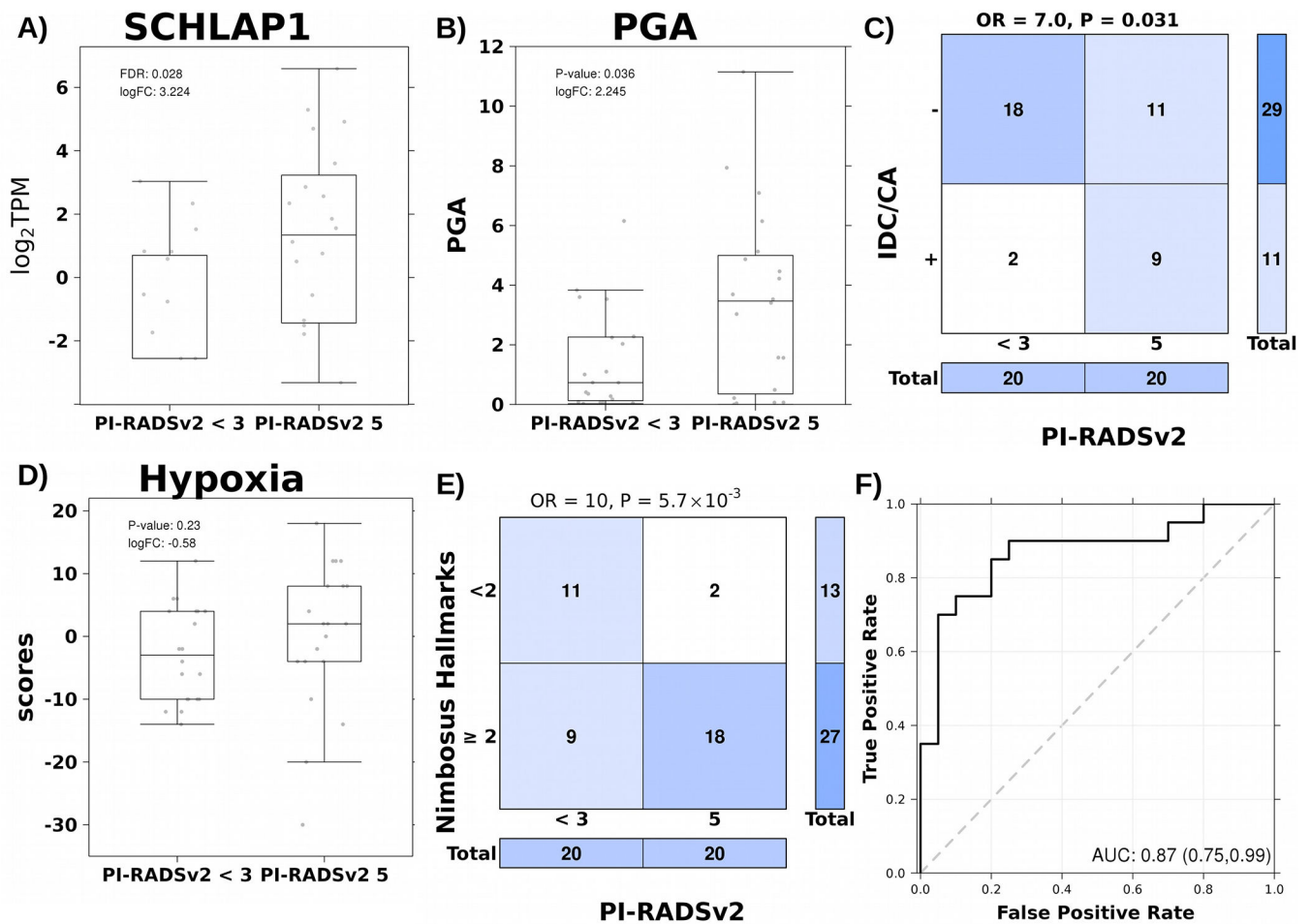
dotmap indicates the enrichment of each RNA. The size of the circle reflects the odds ratio in $\log_2$ space for easier visualization while the colour of the circle reflects if the raw odds ratio is > 1 (red) or < 1 (blue). Finally, the background shading indicates the FDR (Fisher's Exact test). **F)** A snoRNA signature accurately predicted PI-RADSv2 5 tumors with 76% accuracy.

Figure 2 - *Nimbosus* **drives mpMRI visibility**

A) *SCHLAP1* was upregulated in PI-RADSv2 5 tumors as determined from negative binomial generalized log-linear model. Boxplot shows 25% quartile, median and 75% quartile. **B)** PGA was upregulated in PI-RADSv2 5 tumors. P-value from logistic regression adjusting for tumour purity. **C)** IDC/CA was enriched in PI-RADSv2 5 tumors. OR and p-value from Fisher's Exact test. **D)** Hypoxia, quantified using the Ragnum signature[34], was not significantly different between conditions. P-value from Mann-Whitney test. **E)** The co-occurrence of two or more nimbosus hallmarks increased the odds of PI-RADSv2 5 tumor. OR and p-value from Fisher's Exact test. **F)** *Nimbosus* hallmarks synergize with snoRNA signature to accurately predict PI-RADSv2 5 tumours with 87% accuracy.

Table 1 -

Patient characteristics

Summary of patient characteristics selected for mpMRI "invisible" and "visible" groups. P-value from Mann-Whitney test with the exception of pathologic staging and tumor location (Fisher's exact test). Of the characteristics reported, only tumor volume and percent Gleason 4 pattern statistically differ between two groups.

Variables	Invisible lesions (PI-RADSv2 3–5) N=20	Visible lesions (PI-RADSv2 5) N=20	P-value
Age (years)			0.38
median (IQR)	60.5 (54–67)	64 (56–71)	
PSA (ng/mL)			0.35
median (IQR)	6.5 (4.5–7.4)	6.6 (5.0–9.7)	
PSA Density (ng/mL^2)			0.47
median (IQR)	0.15 (0.10–0.2)	0.16 (0.10–0.26)	
Pathologic prostate volume (mL)			0.98
median (IQR)	41 (34–53)	45 (32–52)	
Tumor size (cm)			0.12
median (IQR)	2.1 (1.8–2.7)	2.8 (2.0–3.3)	
Tumor volume (mL)			0.03 *
median (IQR)	4.3 (2.4–7.8)	6.5 (4.5–10.1)	
Pathologic staging (%)			0.05
T2	16 (80)	9 (45)	
T3	4 (20)	11 (55)	
Tumor location (%)			1.00
Peripheral zone	12 (60)	12 (60)	
Transitional zone	8 (40)	8 (40)	
% Gleason 4 pattern (%)			$1.0 \times 10^{-5*}$
1< 5%	5 (25)	0 (0)	
5–10%	12 (60)	5 (25)	
11–30%	3 (15)	8 (40)	
>30%	0 (0)	7 (35)	
% Cribriform architecture (%)			0.09
< 5%	18 (90)	11 (55)	
5–10%	2 (10)	7 (35)	
11–30%	0	2 (10)	
% Intraductal carcinoma (%)			0.42
< 5%	20 (100)	18 (90)	
5–10%	0	1 (5)	
11–30%	0	1 (5)	